2014-8

Resolution-Enhanced All-Optical Analog-to-Digital Converter Employing Cascade Optical Quantization Operation

Zhe Kang
Beijing University of Posts and Telecommunications

Xianting Zhang
Beijing University of Posts and Telecommunications

Jinhui Yuan
Beijing University of Posts and Telecommunications

See next page for additional authors

Recommended Citation

Kang, Z. et al. (2014) Resolution-Enhanced All-Optical Analog-to-Digital Converter Employing Cascade Optical Quantization Operation. *Optics Express,* Vol. 22, Issue 18, pp. 21441-21453. doi:10.1364/OE.22.021441

Funder: This work was supported in part by the National Basic Research Program under Grants 2010CB327605, the National Natural Science Foundation of China under Grant 61307109, the National High-Technology Research and Development Program of China under Grant 2013AA031501, the Specialized Research Fund for the Doctoral Program of Higher Education under Grant 20120005120021, the Fundamental Research Funds for the Central Universities under Grant 2013RC1202, the Program for New Century Excellent Talents in University under Grant NECT-11-0596, the Beijing Nova Program under Grant 2011066, the Hong Kong Scholars Program 2013, the Research Grant Council of the Hong Kong Special Administrative Region China under Grant PolyU5272/12E, and the Science Foundation Ireland (SFI) under Grants SFI/12/ISCA/2496 and SFI/13/ISCA/2845.

Resolution-enhanced all-optical analog-to-digital converter employing cascade optical quantization operation

Zhe Kang,[1] Xianting Zhang,[1] Jinhui Yuan,[1,2,*] Xinzhu Sang,[1] Qiang Wu,[3] Gerald Farrell,[3] and Chongxiu Yu[1]

[1]*State Key Laboratory of Information Photonics and Optical Communications, Beijing University of Posts and Telecommunications, P.O. Box72 (BUPT), 100876, Beijing, China*
[2]*Photonics Research Centre, Department of Electronic and Information Engineering, Hong Kong Polytechnic University, Hung Hom, Kowloon, Hong Kong, China*
[3]*Photonics Research Centre, Dublin Institute of Technology, Kevin Street, Dublin, Ireland*
[*]*yuanjinhui81@163.com*

Abstract: In this paper, a cascade optical quantization scheme is proposed to realize all-optical analog-to-digital converter with efficiently enhanced quantization resolution and achievable high analog bandwidth of larger than 20 GHz. Employing the cascade structure of an unbalanced Mach-zehnder modulator and a specially designed optical directional coupler, we predict the enhancement of number-of-bits can be up to 1.59-bit. Simulation results show that a 25 GHz RF signal is efficiently digitalized with the signal-to-noise ratio of 33.58 dB and effective-number-of-bits of 5.28-bit.

OCIS codes: (230.0250) Optoelectronics; (060.2360) Fiber optics links and subsystems; (070.1170) Analog optical signal processing.

References and links

1. R. H. Walden, "Analog-to-digital converter survey and analysis," IEEE J. Sel. Areas Commun. **17**(4), 539–550 (1999).
2. G. C. Valley, "Photonic analog-to-digital converters," Opt. Express **15**(5), 1955–1982 (2007).
3. A. Khilo, S. J. Spector, M. E. Grein, A. H. Nejadmalayeri, C. W. Holzwarth, M. Y. Sander, M. S. Dahlem, M. Y. Peng, M. W. Geis, N. A. DiLello, J. U. Yoon, A. Motamedi, J. S. Orcutt, J. P. Wang, C. M. Sorace-Agaskar, M. A. Popović, J. Sun, G. R. Zhou, H. Byun, J. Chen, J. L. Hoyt, H. I. Smith, R. J. Ram, M. Perrott, T. M. Lyszczarz, E. P. Ippen, and F. X. Kärtner, "Photonic ADC: overcoming the bottleneck of electronic jitter," Opt. Express **20**(4), 4454–4469 (2012).
4. Y. Han and B. Jalali, "Photonic Time-stretched analog-to-digital converter: fundamental concepts and practical considerations," J. Lightwave Technol. **21**(12), 3085–3103 (2003).
5. L. P. Hou, E. A. Avrutin, M. H. R. Dylewicz, A. C. Bryce, and J. H. Marsh, "160 GHz passively mode-locked AlGaInAs 1.55 μm strained quantum-well lasers with deeply etched intracavity mirrors," IEEE J. Sel. Top. Quantum Electron. **19**(4), 1100409 (2013).
6. J. Schröder, T. D. Vo, and B. J. Eggleton, "Repetition-rate-selective, wavelength-tunable mode-locked laser at up to 640 GHz," Opt. Lett. **34**(24), 3902–3904 (2009).
7. K. Xu, J. Niu, Y. T. Dai, X. Q. Sun, J. Dai, J. Wu, and J. T. Lin, "All-optical analog-to-digital conversion scheme based on Sagnac loop and balanced receivers," Appl. Opt. **50**(14), 1995–2000 (2011).
8. Y. Wang, H. M. Zhang, Q. W. Wu, and M. Y. Yao, "Improvement of photonic ADC based on phase-shifted optical quantization by using additional modulators," IEEE Photon. Technol. Lett. **24**(7), 566–568 (2012).
9. C. H. Sarantos and N. Dagli, "A photonic analog-to-digital converter based on an unbalanced Mach-Zehnder quantizer," Opt. Express **18**(14), 14598–14603 (2010).
10. S. N. Yang, C. Wang, H. Chi, X. M. Zhang, S. L. Zheng, X. F. Jin, and J. P. Yao, "Photonic analog-to-digital converter using Mach-Zehnder modulators having identical half-wave voltages with improved bit resolution," Appl. Opt. **48**(22), 4458–4467 (2009).
11. Y. Miyoshi, S. Takagi, S. Namiki, and K. I. Kitayama, "Multiperiod PM-NOLM with dynamic counter-propagating effects compensation for 5-bit all-optical analog-to-digital conversion and its performance evaluations," J. Lightwave Technol. **28**(4), 415–422 (2010).
12. Y. Miyoshi, S. Namiki, and K. I. Kitayama, "Performance evaluation of resolution-enhanced ADC using optical multiperiod transfer functions of NOLMs," IEEE J. Sel. Top. Quantum Electron. **18**(2), 779–784 (2012).
13. Y. Wang, H. M. Zhang, Y. J. Dou, and M. Y. Yao, "Experimental evaluation of resolution enhancement of a phase-shifted all optical analog-to-digital converter using an electrical analog-to-digital converter array," Chin. Opt. Lett. **11**(8), 082301 (2013).

#215151 - $15.00 USD Received 2 Jul 2014; revised 11 Aug 2014; accepted 13 Aug 2014; published 27 Aug 2014

14. W. Shile, W. Jian, Z. Lingjuan, Y. Chen, J. Chen, L. Dan, Z. Xilin, and Y. Zuoshan, "Multimode interference coupler based photonic analog-to-digital conversion scheme," Opt. Lett. **37**(17), 3699–3701 (2012).
15. H. Chi, Z. Li, X. Zhang, S. Zheng, X. Jin, and J. P. Yao, "Proposal for photonic quantization with differential encoding using a phase modulator and delay-line interferometers," Opt. Lett. **36**(9), 1629–1631 (2011).
16. T. Satoh, K. Takahashi, H. Matsui, K. Itoh, and T. Konishi, "10-GS/s 5-bit real-time optical quantization for photonic analog-to-digital conversion," IEEE Photon. Technol. Lett. **24**(10), 830–832 (2012).
17. T. Konishi, K. Takahashi, H. Matsui, T. Satoh, and K. Itoh, "Five-bit parallel operation of optical quantization and coding for photonic analog-to-digital conversion," Opt. Express **19**(17), 16106–16114 (2011).
18. K. Takahashi, H. Matsui, T. Nagashima, and T. Konishi, "Resolution upgrade toward 6-bit optical quantization using power-to-wavelength conversion for photonic analog-to-digital conversion," Opt. Lett. **38**(22), 4864–4867 (2013).
19. Z. Kang, J. H. Yuan, Q. Wu, T. Wang, S. Li, X. Z. Sang, C. X. Yu, and G. Farrell, "Lumped time-delay compensation scheme for coding synchronization in the nonlinear spectral quantization-based all-optical analog-to-digital conversion," IEEE Photon. J. **5**(6), 7201109 (2013).
20. Z. Kang, J. H. Yuan, S. Li, S. L. Xie, B. B. Yan, X. Z. Sang, and C. X. Yu, "Six-bit all-optical quantization using photonic crystal fiber with soliton self-frequency shift and pre-chirp spectral compression techniques," Chin. Phys. B **22**(11), 114211 (2013).
21. T. Nishitani, T. Konishi, and K. Itoh, "Resolution improvement of all-optical analog-to-digital conversion employing self-frequency shift and self-phase-modulation induced spectral compression," IEEE J. Sel. Top. Quantum Electron. **14**(3), 724–732 (2008).
22. E. L. Wooten, R. L. Stone, E. W. Miles, and E. M. Bradley, "Rapidly tunable narrowband wavelength filter using $LiNbO_3$ unbalanced Mach-Zehnder Interferometers," J. Lightwave Technol. **14**(11), 2530–2536 (1996).
23. D. S. Smith, H. D. Riccius, and R. P. Edwin, "Refractive indices of lithium niobate," Opt. Commun. **17**(3), 332–335 (1976).
24. IEEE Instrumentation and Measurement Society, "IEEE standard for terminology and test methods for analog-to-digital converters," IEEE Std 1241–2010 (2011).
25. IEEE Instrumentation and Measurement Society, "IEEE standard for Digitizing Waveform Recorders," IEEE Std 1057–1994(R2001) (2001).
26. M. Mangold, S. M. Link, A. Klenner, C. A. Zaugg, M. Golling, B. W. Tilma, and U. Keller, "Amplitude noise and timing jitter characterization of a high-power mode-locked integrated external-cavity surface emitting laser," IEEE Photon. J. **6**(1), 1500309 (2014).
27. H. Nasu, T. Takagi, M. Oike, T. Nomura, and A. Kasukawa, "Ultrahigh wavelength stability through thermal compensation in wavelength-monitor integrated laser modules," IEEE Photon. Technol. Lett. **15**(3), 380–382 (2003).
28. H. Nasu, T. Takagi, T. Shinagawa, M. Oike, T. Nomura, and A. Kasukawa, "A highly stable and reliable wavelength monitor integrated laser module design," J. Lightwave Technol. **22**(5), 1344–1351 (2004).

1. Introduction

The high performance analog-to-digital converters (ADCs) have been widely applied in the high speed optical communication, advanced radar system, and real-time signal monitoring. Limited by the inherent aperture jitter and comparator ambiguity, it is difficult to realize an ADC with multi-bit resolution and bandwidth over several tens of GHz by using conventional electronic devices [1–4]. "Photonic ADC" is known to be a potential technology to overcome the limitations of electrical devices and realize ultra-wide bandwidth digitization. Benefit from the development of mode-locked technique, the optical sampling pulse trains with the repetition rate of over hundreds of GSa/s can be realized [5, 6], which can provide ultra-high speed optical sampling with 3~4 orders of magnitude lower timing jitter than that of electrical sampling. The photonic-assisted ADCs that using optical sampling and electrical quantization have exhibited high digitization performance [3, 4]. Especially the results obtained in [3] give the state of the art 41 GHz analog bandwidth with 7 effective number of bits (ENOB). However, the undersampling technique is required for such ultrahigh analog bandwidth because the quantization in [3] is executed completely by electrical ADCs. The undersampling technique is limited to the sampling of narrow-band signals. Thus, the bandwidth limitation of electrical ADCs is inevitable when broadband signals or multitone signals are used for digitization. In order to efficiently connect the optical sampling module and eliminate the electrical bandwidth limitation, it is essential to realize the all-optical operation in both quantization and coding modules. Extensive optical quantization schemes have been proposed and improved aiming to achieve high quantization resolution, e.g. the phase quantization by the modulation and interference [7–15] and the frequency quantization by the nonlinear effects in highly nonlinear fibers [16–21]. In these schemes, the cascade quantization methods demonstrated in [12] and [13] have great advantages compared to the

#215151 - $15.00 USD Received 2 Jul 2014; revised 11 Aug 2014; accepted 13 Aug 2014; published 27 Aug 2014

other schemes because the enhancement of more than 1-bit in the quantization resolution can be obtained on the basis of the conventional phase quantization schemes. However, the second-stage quantization in both of the schemes still rely on the assistance of electrical ADCs. Thus, the bandwidth of input electrical analog signal is limited by the bandwidth of electrical ADCs, which is dominated by the track-and-hold (T/H) circuit. This is because the bandwidth of electrical ADCs should be at least 2.5 times of the maximum frequency of the analog signal to capture it with the minimal amplitude error. For example, to digitize a 25 GHz analog signal, the electrical ADCs with no less than 62.5 GHz bandwidth are required as the second-stage quantizers, which is difficult in practice. The analog bandwidths demonstrated in [12] and [13] are both 10 GHz so that the electrical ADCs with the bandwidth of more than 25 GHz are required. To the best of our knowledge, there is still no reports on the cascade quantization with all-optical process in both of the quantization stages.

In this paper, we propose an all-optical ADC with the enhanced resolution based on a cascade optical quantization (COQ) scheme, which employs an unbalanced Mach-zehnder modulator (UMZM) and a specially designed optical directional coupler. Since the entire quantization operates in all-optical process, the bandwidth limitation of electrical ADCs is eliminated. Simulations show that a 25 GHz sinusoidal analog signal can be efficiently digitized using the proposed scheme.

2. Principle of operation

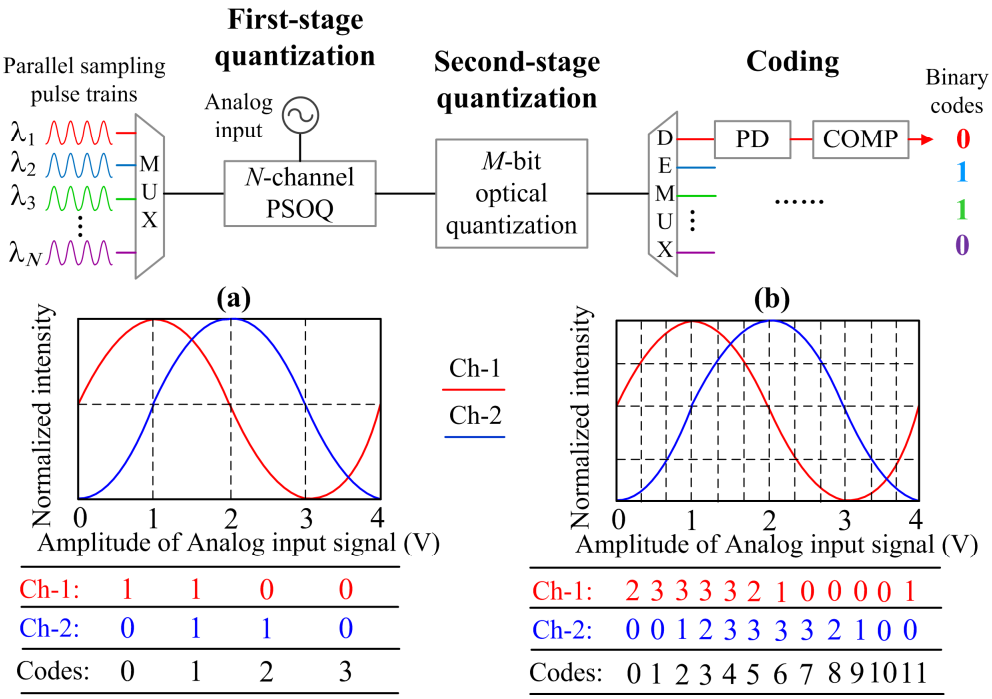

Fig. 1. Schematic diagram of the proposed COQ-ADC. Inset (a) illustrates the power transfer function and coding results of the first-stage quantization in the case of two channels ($N = 2$), and inset (b) illustrates the combined power transfer function and coding results of the two quantization stages with $N = 2$ and $M = 2$. PSOQ: phase-shifted optical quantization; Mux: multiplexer; Demux: demultiplexer; PD: Photodiodes; COMP: comparator.

The schematic diagram of the proposed COQ-ADC is shown in Fig. 1. The parallel optical pulse trains with N different wavelengths are launched from a tunable mode-locked laser source and used as the N-channel sampling pulse source. In the time domain, the pulses at the different wavelengths are superposed on each other at the same time. Together with the electrical analog signal, the sampling pulse trains are delivered into the first-stage

#215151 - $15.00 USD Received 2 Jul 2014; revised 11 Aug 2014; accepted 13 Aug 2014; published 27 Aug 2014

quantization module for sampling and quantization. The first-stage quantization module implements the N-channel phase-shifted optical quantization (PSOQ) and provides N different sinusoidal power transfer functions corresponding to the different channels. When it is directly followed by the photo detection and binary decision, the PSOQ module provides the number of bits (NOB) of $\log_2(2N)$-bit [7, 8]. The inset (a) of Fig. 1 shows the power transfer functions and the coding results of the PSOQ module in the case of two channels. It is evident that a 2-bit resolution is obtained with the combination of the coding results of two channels. Instead of the detection and binary decision, a M-bit optical quantization module is used in our scheme to further quantize the output power of the PSOQ module. Benefit from the second-stage quantization, the quantization level can be further increased. In the case of M = 2, as shown in the inset (b) of Fig. 1, the quantization level is increased from 4 to 12 without adding additional channels. After the two-stage quantization, the output parallel pulse trains are de-multiplexed and delivered into the photodiodes and comparators for the detection and binary decision separately. The NOB of the proposed COQ-ADC is $\log_2[2N(2^M-1)]$-bit, which means the enhancement of $\log_2(2^M-1)$-bit is achieved compared to the conventional PSOQ. The performance of resolution enhancement is shown in Fig. 2. It is evident that the NOB increases efficiently with M. However, for the case of $M > 2$, the lengths of quantization levels cannot be constant due to the nonlinear variation of sinusoid. This problem leads to the severe degradation on the ENOB without considering any other quantization noises, and even makes the resolution enhancement lower than the case of M = 2 [13]. In order to ensure the constant length of quantization levels in the initial stage, M = 2 is used in this scheme which provides the resolution enhancement of $\log_2(2^2\text{-}1)$ = 1.59-bit.

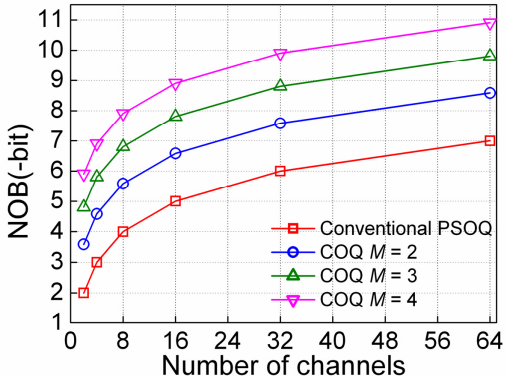

Fig. 2. Performance of resolution enhancement with different M.

The PSOQ module is realized by a lithium niobate UMZM, as shown in Fig. 3(a). The UMZM consists of two Y-junctions, two transmission arms with different geometric path lengths, electrodes, and $LiNbO_3$ substrate. In consideration of the TE mode input, the power transfer function of the UMZM can be obtained as [9, 22]

$$H(t)=\frac{\left[1+\cos\left(\frac{\pi V(t)}{V_\pi}+\frac{2\pi n_e \Delta L}{\lambda}\right)\right]}{2} \tag{1}$$

where $V(t)$ is the amplitude of the input analog signal, V_π is the half-wave voltage of the modulator, ΔL is the geometric path length imbalance of the UMZM, $n_e(\lambda)$ is the refractive index of the $LiNbO_3$ for TE mode calculated by the Sellmeier equation [23]. It is evident that a wavelength-dependent extra phase shift $2\pi n_e \Delta L/\lambda$ is introduced in addition to the modulation phase shift $\pi V(t)/V_\pi$. For the case of ΔL = 40 μm, the extra phase shift as a function of input wavelength is shown in Fig. 3(b). It can be found that the variation of extra phase shifts is quite linear with the wavelengths. Within the wavelength range of 1.54 to 1.56

#215151 - $15.00 USD Received 2 Jul 2014; revised 11 Aug 2014; accepted 13 Aug 2014; published 27 Aug 2014

μm, the total amount of phase shift variation is 1.5π. By properly selecting N sampling pulse trains at specific wavelengths, the differences of the extra phase shift between adjacent wavelengths can be π/N. The N power transfer functions with the identical phase shift gap of π/N can realize the PSOQ with NOB of $\log_2(2N)$-bit.

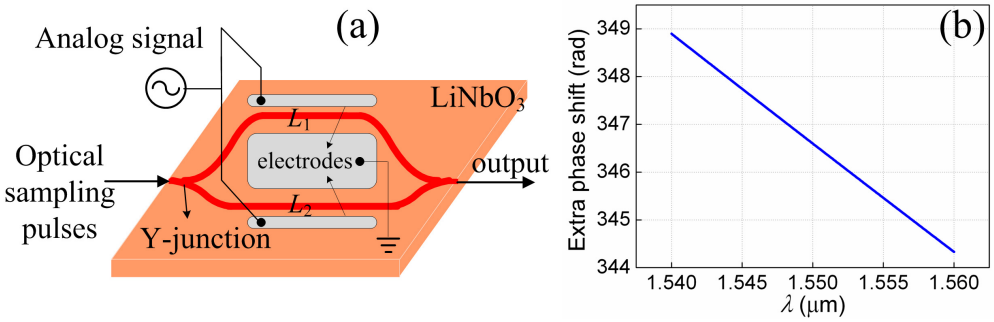

Fig. 3. (a) The structure of UMZM, and (b) extra phase shift as a function of input wavelength (ΔL = 40 μm, wavelength range: 1.54~1.56 μm).

3. Design of the second-stage quantization module

According to the discussion above, a 2-bit optical quantizer is necessary for the second-stage quantization. A GaAs/AlGaAs waveguide based directional coupler is designed, which is composed of three cascaded 2 × 2 directional couplers with different power splitting ratios of 1:1, 1:1, and 2:1, respectively. Figure 4(a) represents the structure of the directional coupler. The core region is made of GaAs while the cladding region is AlGaAs with an aluminium fraction of 20%. The propagation length of the coupler is set to be L_0 = 7.4 mm. Three coupling regions signed as A, B, and C are carried out in this coupler, which have the same length of L = 0.75 mm. The branching angles are all set to be β = 45°. The widths of the waveguides are defined as w_1 and w_2, and the gaps of the waveguides are d_1, d_2, and d_3, respectively. By carefully configuring the widths and gaps, the expected power splitting ratios of 1:1, 1:1, and 2:1 can be realized for three coupling regions.

The output signals of the UMZM experience three-stage power splitting in the directional coupler and are detected at port1, 2, and 3 for the binary decision. Assuming the power of the output signal of the UMZM (i.e. the input of the coupler) is P_0, the detected powers at port1, 2, and 3 should be $P_0/2$, $P_0/4$, and $P_0/6$, respectively. The power transfer functions and coding results of the directional coupler are shown in Fig. 4(b), where $P_{0\text{-max}}$ is the maximum of P_0, and P_{th} is the threshold for binary decision which meets $P_{th} = P_{0\text{-max}}/8$. When the insertion loss α is considered, the threshold should be modified to $P_{th}' = (10^{-\alpha/10} \times P_{0\text{-max}})/8$. It is evident that the power of the output pulse of the UMZM can be further divided into four uniform levels with the binary codes of "000", "100", "110", and "111", which means a 2-bit quantization is realized. In the case of symmetric structure ($w_1 = w_2$), the power splitting ratio of the directional coupler changes severely with the wavelength of input optical wave. Since the multiple channels with the wavelengths among 1.54~1.56 μm are required in this scheme, the directional coupler with the asymmetric structure is designed, i.e. w_1 = 0.8 μm and w_2 = 1 μm. d_1, d_2, and d_3 are correspondingly set at 2.8 μm, 2.8 μm, and 2.6 μm so that the specific power splitting ratios of 1:1, 1:1, and 2:1 can be obtained. By using the beam propagation method (BPM), the dynamic of the optical field at 1.55 μm is shown in Fig. 5(a). Also the power fraction of different output ports as a function of propagation length is illustrated in Fig. 5(b). It is evident that the power fraction of port1, port2, and port3 are 50.6%, 24.4%, and 15.9%, respectively. Compared with the ideal power fraction, i.e. 50%, 25%, and 16.7%, the small fluctuation of power fraction will lead to the degradation of ENOB.

#215151 - $15.00 USD Received 2 Jul 2014; revised 11 Aug 2014; accepted 13 Aug 2014; published 27 Aug 2014

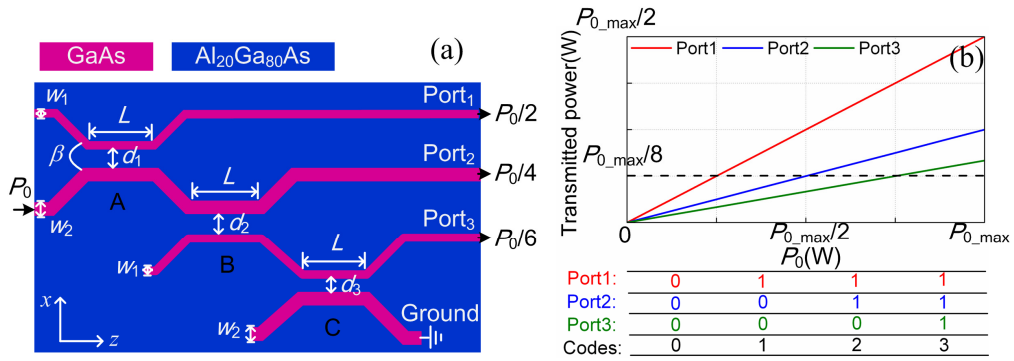

Fig. 4. (a) The structure of the designed directional coupler, and (b) the power transfer functions and coding results of the second-stage quantization.

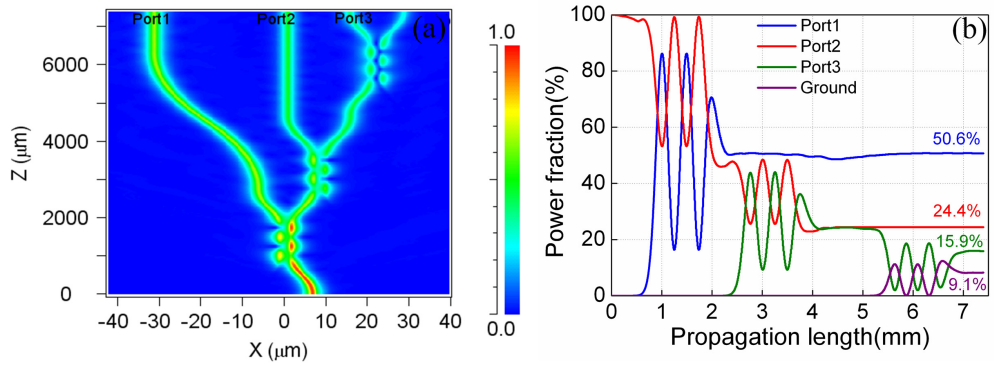

Fig. 5. (a) The dynamic of the optical field along the propagation direction (λ = 1.55 μm), and (b) the power fraction of three output ports and the ground port as a function of the propagation length.

The power fraction of different ports as a function of input wavelength is illustrated in Figs. 6(a)–6(c). Both the asymmetric and symmetric structures are considered to confirm the wavelength-insensitive of the coupler designed. For the case of the symmetric structure, the power fraction of port1 and port3 changes evidently with the wavelength while the change of port2 is relatively small. The small change of port2 is mainly due to the same structure of the coupling regions A and B, which mitigates the change of power fraction at the port2. By contrast, for the asymmetric structure, the changes of power fraction at three output ports are all quite small within the wavelength range of 1.54~1.56 μm. The wavelength-insensitive characteristic can efficiently mitigate the degradation of ENOB compared to the case of symmetric structure. The power fluctuation is defined as the absolute value of the difference between the detected power fraction and the ideal power fraction. Figure 6(d) shows the power fluctuations of three output ports as a function of input wavelength in the cases of the symmetric and asymmetric structures. It is evident the power fluctuations of the proposed asymmetric structure are all less than 1% within the wavelength range considered while the fluctuation of larger than 8% is found in the symmetric structure.

#215151 - $15.00 USD Received 2 Jul 2014; revised 11 Aug 2014; accepted 13 Aug 2014; published 27 Aug 2014

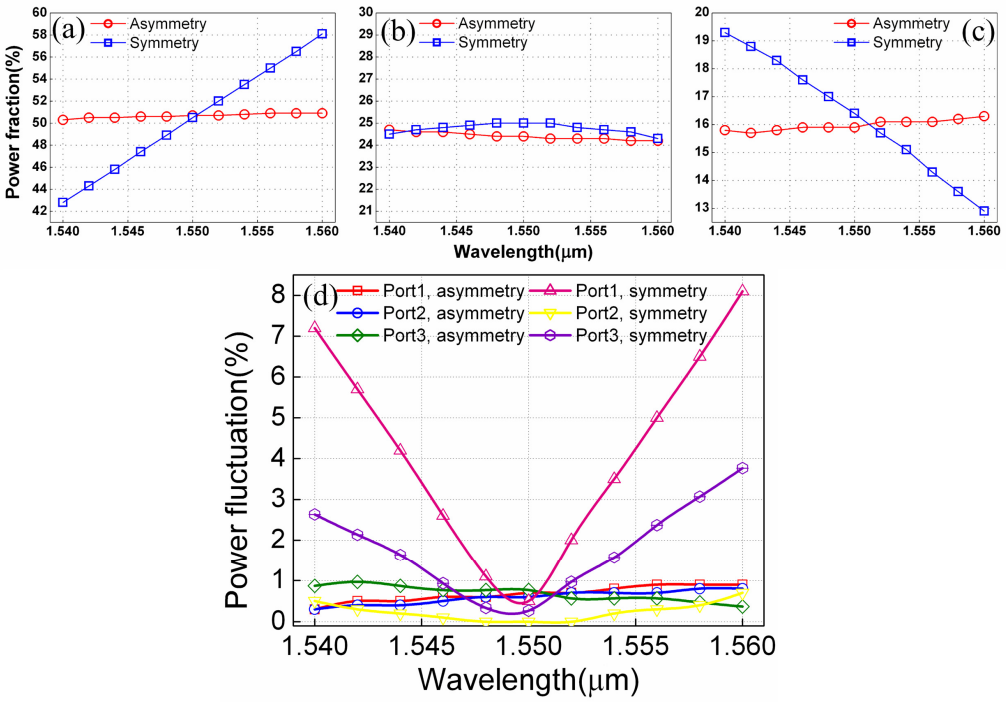

Fig. 6. The calculated power fraction of the symmetric and asymmetric structures as a function of input wavelength at (a) port1, (b) port2, and (c) port3, respectively. (d) the power fluctuations of the symmetric and asymmetric structures as a function of input wavelength at different output ports.

4. Performance of digitization

In the simulation, a 25 GHz sinusoidal wave signal is used as the electrical analog signal, and pre-amplified to the peak-to-peak power of $2V_\pi$. Since there is no nonlinear effect in this scheme, the tunable continuous wave (CW) source with peak power of 8 mW and the software sampling are used instead of the pulsed source. The software sampling can be achieved by extracting the detected electrical waveforms with a fixed time interval. Eight wavelengths are selected according to the discussion in section2 to realize the eight quantization channels, which can achieve the NOB of 5.59-bit. The eight wavelengths and corresponding phase-shifts are illustrated in Table 1. The wavelength interval is found to be 1.7 nm. This interval is large enough for avoiding the spectral overlap when the pulsed source with the pulse width of several picoseconds is used for sampling. Also, the wavelength interval can be flexibly adjusted by changing the ΔL of the UMZM so that it can be applied to the sampling pulse width of femtosecond magnitude. Together with the electrical analog signal, the eight parallel optical carriers are delivered into the UMZM, which has the V_π = 3.3 V and ΔL = 40 μm. The temporal profiles of the sinusoidal wave signal and the output signal of the UMZM are shown in Figs. 7(a) and 7(b). Three channels with the extra phase-shifts of $\pi/8$, $4\pi/8$, and $7\pi/8$ are illustrated. The temporal profiles are demonstrated within two periods. Since the frequency of the analog signal is 25 GHz, the length of the period is 40 ps. It is evident that different "M" curves are obtained due to the different power transfer functions of the channels. The output signals of the UMZM are further delivered into the directional coupler for the second-stage quantization. After the quantization process, the optical signals are detected at the port1, 2, and 3 of the coupler, respectively. Taking λ_4 as an example, i.e. the extra phase-shift is $3\pi/8$, the detected waveforms are shown in Figs. 8(a)–8(c).

#215151 - $15.00 USD Received 2 Jul 2014; revised 11 Aug 2014; accepted 13 Aug 2014; published 27 Aug 2014

Table 1. Selected Wavelengths and Corresponding Phase-shifts

λ(nm)	1548	1549.7	1551.4	1553.1	1554.8	1556.6	1558.3	1560
$\Delta\varphi(\lambda)$	0	π/8	2π/8	3π/8	4π/8	5π/8	6π/8	7π/8

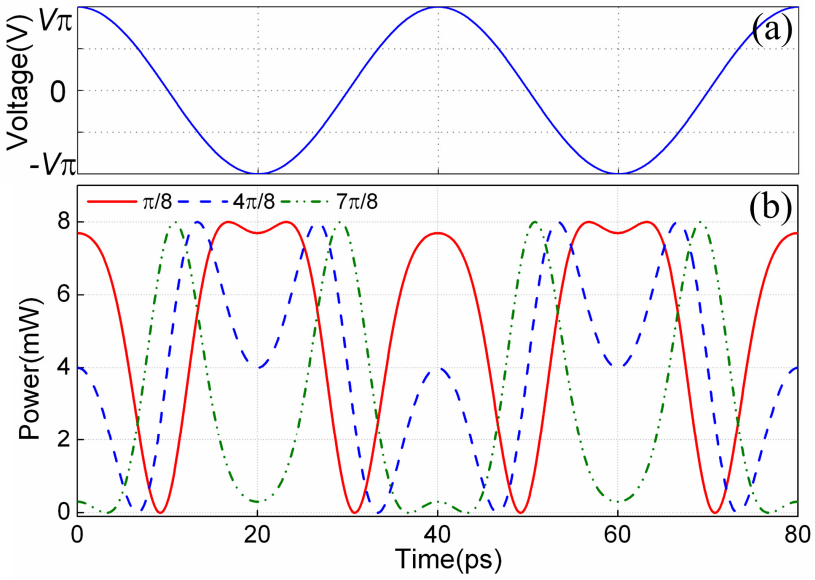

Fig. 7. (a) Input sinusoidal wave signal, and (b) the output temporal profiles of the UMZM.

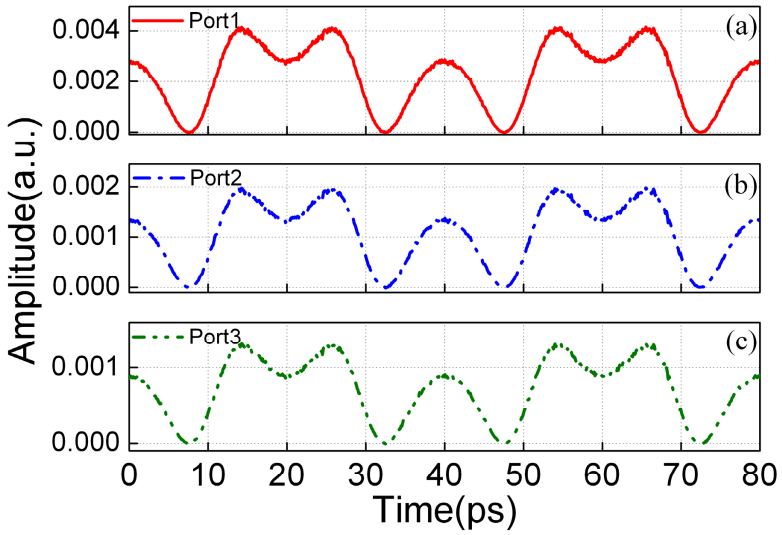

Fig. 8. The detected waveforms at (a) port1, (b) port2, and (c) port3 of the directional coupler.

The fluctuation of the amplitude is caused by the thermal noise and shot noise of the photodiode considered in the simulation. Besides the power splitting fluctuation discussed in section3, this detection noises also lead to the degradation of the ENOB. The detected waveforms are subsequently software sampled with a specific time interval. The sampled points are finally made binary decision by an identical threshold and encoded. Combining the encoding results of the eight channels, the digitized values and corresponding sinusoidal-

#215151 - $15.00 USD Received 2 Jul 2014; revised 11 Aug 2014; accepted 13 Aug 2014; published 27 Aug 2014

fitted curve are illustrated in Fig. 9(a). The errors between the digitized values and the fitted curve are also calculated and shown in Fig. 9(b). It can be found the maximum of the errors is around 1 least significant bit (LSB). Using the root-mean-square (RMS) of the errors, the signal-to-noise ratio (SNR) of 33.58 dB and the ENOB of 5.28-bit are obtained, which are estimated by Eqs. (2) and (3) [8, 24, 25]

$$SNR \approx \frac{RMS\_signal}{RMS\_errors} = \frac{A/\sqrt{2}}{\sqrt{\frac{1}{M}\sum_{n=1}^{M}\left(y_n - y_n'\right)^2}} \tag{2}$$

$$ENOB = \frac{SNR - 1.76}{6.02} \tag{3}$$

where A is the peak amplitude of the fitted sine curve, M is the number of samples, y_n and y_n' are the n-th data of the digitized results and the fitted curve, respectively. Affected by the power splitting fluctuation of the directional coupler and the detection noises, the degradation of ENOB is 0.39-bit.

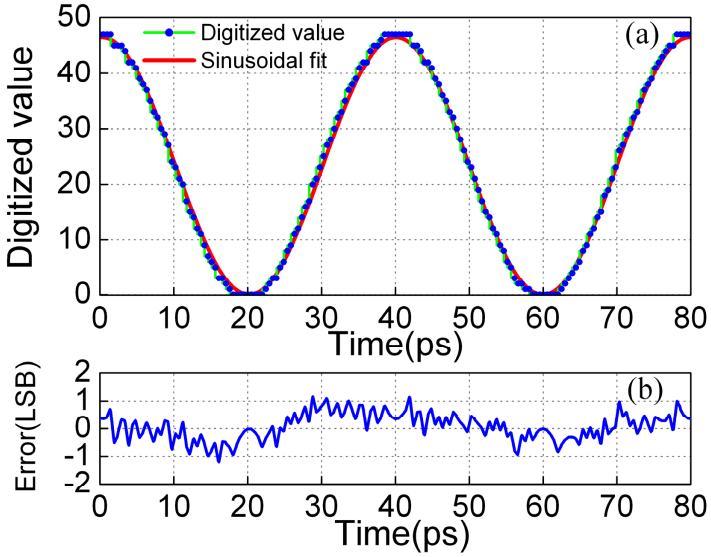

Fig. 9. (a) The digitized result and sinusoidal fitted curve, and (b) the errors between the digitized values and the fitted curve.

5. Discussion

In the practical case, other effects like the timing jitter and the random intensity noise (RIN) of the pulsed source, the phase jitter of the power transfer function of the UMZM, and the walk-off of different channels in the UMZM should also be considered besides the power splitting fluctuation and detection noises considered above to confirm the feasibility of the proposed COQ-ADC.

A. Timing jitter and RIN

In the practical applications, the pulsed source can be used instead of the CW source and software sampling. The timing jitter of the pulsed source will lead to the amplitude deviation between the practical and ideal sampling points. Assuming an input sinusoidal signal with the peak amplitude of A and frequency of f, the amplitude deviation δA induced by the timing jitter τ can be given by Eq. (4)

$$\delta A = A\sin\left[2\pi f\left(t+\tau\right)\right] - A\sin\left(2\pi ft\right) \tag{4}$$

In general, $\tau << 1$ ns is satisfied so that the Eq. (4) can be simplified to

#215151 - $15.00 USD Received 2 Jul 2014; revised 11 Aug 2014; accepted 13 Aug 2014; published 27 Aug 2014

$$\delta A = 2\pi fA \cdot \tau \cdot \cos(2\pi ft) \tag{5}$$

The tolerated amplitude deviation should be no more than $\Delta/2$. Here, $\Delta = 2A/2^{NOB}$ is the amount of the LSB. Thus, the maximum of the tolerated timing jitter can be obtained as

$$\tau_{max} = \left(2^{NOB+1} \cdot \pi \cdot f\right)^{-1} \tag{6}$$

τ_{max} as a function of the input frequency is shown in Fig. 10(a). The input frequency of the signal is related to the analog bandwidth of the ADC. It is evident that the timing jitter decreases greatly with the increase of the analog bandwidth and the quantization resolution. Since the NOB and analog bandwidth of the proposed scheme are 5.59-bit and 25 GHz, the timing jitter should be no more than 132.2 fs. Fortunately, the low timing jitter of less than several tens of femtoseconds is achievable using the existing mode-locked laser diodes [3]. Thus, the analog bandwidth of the proposed scheme limited by the timing jitter can be up to 100 GHz. Besides the timing jitter, the analog bandwidth of the proposed COQ-ADC is also limited by the bandwidths of the optical modulator and detector. The commercial $LiNbO_3$ modulators and photodiodes with the bandwidths of no less than 40 GHz are common. Also, for the applications of beyond 100G ultra-high speed optical communications system and millimeter-wave radio-over-fiber system, the bandwidth of even 100 GHz can be realized. Therefore, the proposed COQ-ADC has the potential to achieve the high analog bandwidth of larger than 100 GHz.

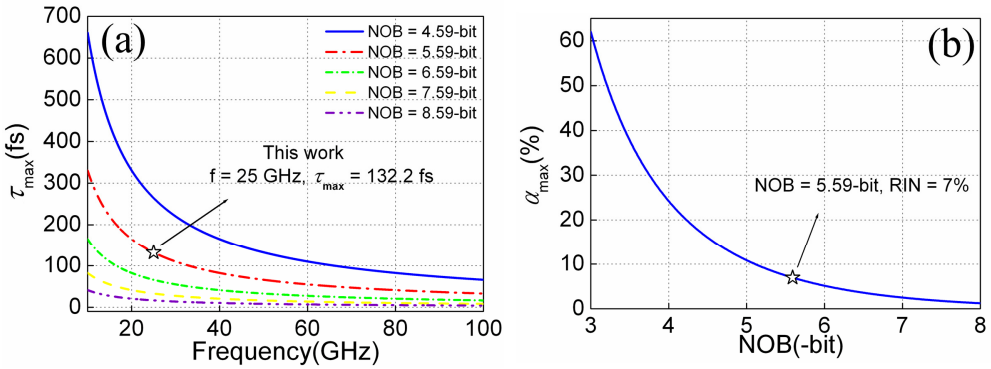

Fig. 10. (a) τ_{max} as a function of the input frequency with different NOB, and (b) α_{max} as a function of the NOB.

The RIN-induced intensity jitter of the sampling pulses can lead to the error of binary decision and corresponding quantization errors. The RIN can be defined as $\alpha = \Delta P/P_0$. Here, ΔP is the intensity jitter and P_0 is the original intensity of the pulses. Due to the sinusoidal power transfer function, the output power of the UMZM without effects of RIN can be defined as $P = P_0(\sin\theta + 1)/2$, $\theta \in [0, 2\pi]$. This definition is just a simplified expression and corresponding discussion can be extended to Eq. (1). When the RIN exists, the output power changes to $P = (P_0 + \Delta P)(\sin\theta + 1)/2$. The power change induces the error of binary decision, and corresponding quantization error Δ_1 can be given by

$$\Delta_1 = \arcsin\left(\frac{\alpha}{1+\alpha}\right) \cdot \frac{P_{FS}}{2\pi} \tag{7}$$

where P_{FS} is the full-scale power of the analog signal and can be represented by the LSB as $2^{NOB} \times \Delta$. Similar to the timing jitter, Δ_1 should be no more than $\Delta/2$. Thus, the tolerated RIN is given by

$$\alpha < \frac{\sin\left(\pi / 2^{NOB}\right)}{1 - \sin\left(\pi / 2^{NOB}\right)} \tag{8}$$

#215151 - $15.00 USD Received 2 Jul 2014; revised 11 Aug 2014; accepted 13 Aug 2014; published 27 Aug 2014

The maximum RIN α_{max} as a function of the NOB is shown in Fig. 10(b). It is evident the tolerated RIN decrease rapidly with the NOB. For the NOB = 5.59-bit in our proposed scheme, the maximum RIN is about 7%. Since the ultralow RIN of less than 0.15% has been reported to be achievable [26], the digitization performance of our proposed scheme would not be degraded severely by the RIN.

B. Phase jitter

The phase jitter is probably induced by the wavelength fluctuation of the selected channels, and leads to the offset of the power transfer functions of the UMZM. The offset can directly induce the non-uniform of the quantization steps and generate the quantization error. This quantization error is defined as Δ_2, which can be calculated via $\Delta_2 = \delta\theta \times P_{FS}/2\pi$ in this scheme. Here, $\delta\theta$ is the phase jitter. Since the offset of one power transfer function can generate 2 × 3 quantization errors, the ENOB as a function of $\delta\theta$ can be calculated using Eq. (9)

$$ENOB = \frac{SNR - 1.76}{6.02} = 10\log_{10}\left\{\frac{\left(P_{FS}/2\sqrt{2}\right)^2}{\frac{1}{P_{FS}}\left[\sum_{i=1}^{N} 2\times 3\times\left(\int_0^{\Delta/2+\Delta_{2\_i}} p^2 dp + \int_{\Delta/2+\Delta_{2\_i}}^{\Delta} (p-\Delta)^2 dp\right)\right]}\right\} - 1.76 \Big/ 6.02 \quad (9)$$

where Δ_{2_i} is the quantization error of i-th channel. The ENOB calculated as a function of the phase jitter is shown in Fig. 11. It can be seen that the ENOB decreases with the increase of $\delta\theta$. And the ENOB with the higher resolution is much more sensitive to the change of $\delta\theta$ because the quantization steps become narrower. The tolerated phase jitter is given by

$$\frac{2\cdot 3\cdot \delta\theta \cdot P_{FS}}{2\pi} < \frac{\Delta}{2} \quad (10)$$

From the Eq. (10), the maximum of $\delta\theta$ is found to be $\pi/36N$. Because of $N = 8$ in this scheme, the tolerated phase jitter should be less than 0.0109 rad. This phase jitter is corresponding to the maximum wavelength fluctuation of 47.7 pm. For the applications in the dense wavelength-division multiplexing system, the commercial laser sources with wavelength fluctuation of less than 5 pm can be realized [27, 28]. This value is an order of magnitude lower than the tolerated value of 47.7 pm, which confirms that the proposed COQ-ADC has good ability to tolerate the phase jitter noise.

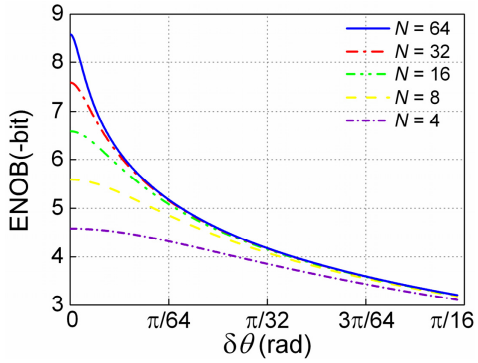

Fig. 11. The ENOB of the proposed COQ-ADC as a function of the phase jitter with different number of channels.

#215151 - $15.00 USD Received 2 Jul 2014; revised 11 Aug 2014; accepted 13 Aug 2014; published 27 Aug 2014

C. Walk-off effect

When the pulsed source is used, two optical waves propagating in the upper and lower arms of the UMZM have the optical path difference (OPD) due to the geometric path length imbalance of the UMZM. The OPD will lead to the walk-off between two optical waves which interfere with each other at the output of the UMZM. When the walk-off is comparable to the pulse width, the interference effect will get worse, i.e. the performance of quantization will be degraded. The amount of walk-off can be calculated by $\delta t = \beta_1(\lambda)\Delta L$. Here, $\beta_1(\lambda)$ is the first-order dispersion parameter of the $LiNbO_3$ UMZM which is reciprocal of the group velocity, and ΔL is the length difference of the upper and lower arms of the UMZM. $\beta_1(\lambda)$ can be obtained using the refractive index of the $LiNbO_3$ as discussed in section2. For the wavelength range of 1.548~1.56 μm and ΔL = 40 μm in this scheme, the amounts of walk-off and $\beta_1(\lambda)$ as a function of wavelength are illustrated in Fig. 12(a). Both of the walk-off and $\beta_1(\lambda)$ change slightly with the wavelength. The maximum of δt is found to be 291.042 fs. This value is negligible for the pulse width of several picoseconds. Such picoseconds pulse can theoretically provide the sampling rate of several hundreds of GHz, which is large enough for the Nyquist sampling of the analog signal with several tens of GHz bandwidth. Therefore, the walk-off effect induced by the geometric path length imbalance of the UMZM can be neglected in this proposed scheme.

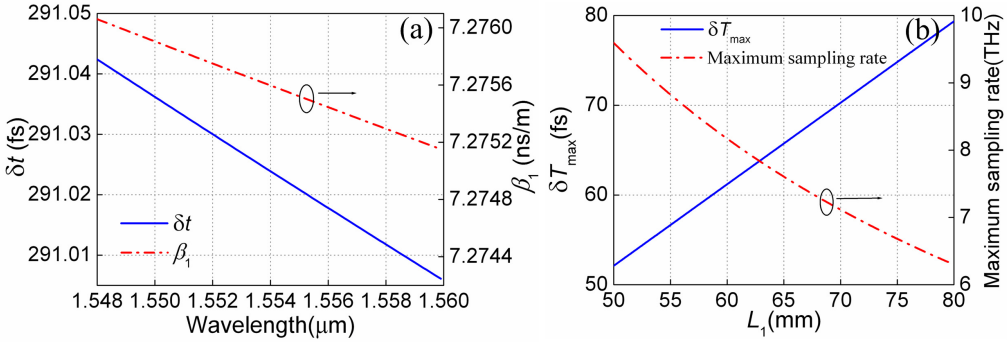

Fig. 12. (a) The amounts of walk-off and $\beta_1(\lambda)$ as a function of wavelength, and (b) the maximum amount of the inter-channel walk-off and supportable maximum sampling rate as a function of the length of UMZM.

Since the sampling channels with multiple wavelengths are required in the proposed scheme, the walk-off among different channels also exists during the transmission. This inter-channel walk-off effect can lead to the non-synchronization of the parallel decision sequences and generate wrong encoding results. To avoid the encoding error, the amount of the inter-channel walk-off should satisfies

$$\delta T \le \frac{1}{2R_s} = \frac{T}{2} \tag{11}$$

where δT is the amount of the walk-off, R_s is the sampling rate, and T is the interval between adjacent sampling pluses. δT can be calculated by Eq. (12)

$$\delta T = \left[\beta_1(\lambda_i) - \beta_1(\lambda_j)\right] \cdot (L_1 + L_2) \qquad i, j \in 1,2...N; i \ne j \tag{12}$$

where λ_i and λ_j are the wavelengths of i-th and j-th channels, respectively, L_1 is the length of the UMZM, and L_2 is the length of directional coupler. L_1 is usually within the range of several tens of millimeters while L_2 is 7.4 mm. Due to the linear variation of β_1 in this scheme, the maximum amount of the inter-channel walk-off δT_{max} as a function of L_1 can be obtained, which is shown in Fig. 12(b). It is evident that δT_{max} is no more than 79.4 fs when L_1 is in the range of 50~80 mm. Moreover, the supportable maximum sampling rate (SMSR)

#215151 - $15.00 USD Received 2 Jul 2014; revised 11 Aug 2014; accepted 13 Aug 2014; published 27 Aug 2014

can be obtained by Eq. (11). The SMSR is found to be several THz, which is far beyond the required Nyquist sampling rate of the analog signal with several tens of GHz bandwidth. If the sampling rate of less than the SMSR is used, the inter-channel walk-off effect will show no influence on the encoding correctness. It is easy to satisfy this sampling condition, i.e. the required Nyquist sampling rate should be less than the SMSR, so that the influence of the inter-channel walk-off can be neglected for this proposed COQ-ADC.

Moreover, the nonlinearities of the components, e.g. the amplifier, the modulator, the photodiode, and the comparator, could also induce degradation of the quantization performance. Fortunately, the influence of the nonlinearities can be mitigated by using proper bandpass and lowpass filters [3] so that the ENOB would not be degraded rapidly in practice.

6. Conclusion

In summary, a COQ-ADC is proposed aiming to the all-optical ADC with high resolution and analog bandwidth. The simple cascade structure of an UMZM and a specially designed optical directional coupler is employed to realize all-optical quantization without the bandwidth limitation of electrical ADCs. Benefit from the all-optical process, the high analog bandwidth of more than several tens of GHz is achievable. Compared to the conventional PSOQ schemes, the resolution enhancement can be up to 1.59-bit without using any additional modulation or optical nonlinear process. Such high resolution enhancement enables the NOB of more than 7.59-bit to be achieved, with which the ENOB is potential to be comparable with the state of the art results obtained in [3]. Nevertheless, the advantage of the proposed COQ-ADC is that higher analog bandwidth can be predicted due to the all-optical process and the flexibility to various analog signals but not limited to narrow-band signals. On the other hand, the required number of channels of this COQ-ADC can be triple less than that of the PSOQ schemes in the case of same resolution, e.g. only 8 channels are needed for the resolution of 5.59-bit in the COQ-ADC while 24 channels are needed in the conventional PSOQ schemes. Although the required number of detectors and comparators remains the same, the large reduction of quantization channels can efficiently save the power consumption. A 25 GHz analog signal is illustrated to be digitized by the COQ-ADC, and the NOB of 5.59-bit and ENOB of 5.28-bit are obtained. The influences of the timing jitter, the RIN, the phase jitter, and the walk-off effect on the digitization performances are also discussed to confirm the feasibility of the proposed COQ-ADC. Moreover, the entire components used in this scheme can be realized by silicon photonics technology so that the proposed COQ-ADC has the potential to be integrated on a single chip.

Acknowledgments

This work was supported in part by the National Basic Research Program under Grants 2010CB327605, the National Natural Science Foundation of China under Grant 61307109, the National High-Technology Research and Development Program of China under Grant 2013AA031501, the Specialized Research Fund for the Doctoral Program of Higher Education under Grant 20120005120021, the Fundamental Research Funds for the Central Universities under Grant 2013RC1202, the Program for New Century Excellent Talents in University under Grant NECT-11-0596, the Beijing Nova Program under Grant 2011066, the Hong Kong Scholars Program 2013, the Research Grant Council of the Hong Kong Special Administrative Region China under Grant PolyU5272/12E, and the Science Foundation Ireland (SFI) under Grants SFI/12/ISCA/2496 and SFI/13/ISCA/2845.

#215151 - $15.00 USD Received 2 Jul 2014; revised 11 Aug 2014; accepted 13 Aug 2014; published 27 Aug 2014